Solute strengthening of both mobile and forest dislocations: The origin of dynamic strain aging in fcc metals

M.A. Soare, W.A. Curtin *

Division of Engineering, Brown University, Providence, RI 02912, USA

Abstract

A full rate-dependent constitutive theory for dynamic strain aging is developed based on two key ideas. The first idea is that both solute strengthening and forest strengthening must exist and must exhibit aging phenomena. The second idea is that a single physical aging mechanism, cross-core diffusion within a dislocation core, controls the aging of both the solute and forest strengthening mechanisms. All the material parameters in the model, apart from forest dislocation density evolution parameters, are derivable from atomistic-scale studies so that the theory contains essentially no adjustable parameters. The model predicts the steady-state stress/ strain/strain-rate/temperature/concentration dependent material response for a variety of Al–Mg alloys, including negative strain-rate sensitivity, in qualitative and quantitative agreement with available experiments. The model also reveals the origin of non-additivity of solute and forest strengthening, and explains observed non-standard transient stress behavior in strain-rate jump tests.
© 2008 Acta Materialia Inc. Published by Elsevier Ltd. All rights reserved.

Keywords: Plastic deformation; Aluminum alloys; Strain-rate sensitivity; Dislocations; Constitutive equations

1. Introduction

In a companion paper [1], it was shown that a proper rate theory for thermally activated dislocation motion involving a single rate-dependent dislocation strengthening mechanism is unable to predict a regime of negative strain-rate sensitivity (nSRS), defined as $m = d(\ln(\tau))/d(\ln(\dot{\varepsilon}))$, where τ is the stress, and $\dot{\varepsilon}$ is the strain rate. Previous theories [2–9] have made invalid simplifications in the rate theory and assumptions in the underlying physics such that nSRS is predicted, as discussed in the companion paper, but such theories lack a direct connection to physical mechanisms of dynamic strain aging or to material parameters. Thus, while exhibiting features consistent with experiments, the theories remain phenomenological and are not predictive. Here, the analysis in the companion paper is extended in a crucial way by the incorporation of two concurrent strengthening mechanisms, solute strengthening and forest hardening,

each of which is influenced by the same time-dependent mechanism of cross-core solute diffusion proposed by Curtin et al. [10]. That is, solute diffusion simultaneously influences both (i) temporarily arrested but otherwise mobile dislocations and (ii) forest dislocations formed during the plastic deformation. Solute strengthening controls the overall rate dependence, so that forest hardening enters the theory as a time-, strain- and strain-rate dependent "back-stress" acting on the mobile dislocations. The dynamic solute strengthening of the mobile dislocations assists in achieving overall nSRS by reducing the "normal" positive strain-rate sensitivity (SRS) parameter to nearly zero and also accounts for transients during strain-rate jumps. The dynamic forest strengthening mechanism, previously proposed and analyzed in general by Picu [11,12], provides a nSRS such that the overall SRS is negative over a range of strain rates and temperatures. The present theory of strain aging thus relates the nanoscale solute/dislocation–core interactions to the macroscopic strain-rate behavior through relatively direct analytical expressions. Assuming a strain-dependent evolution of the forest

---

* Corresponding author. Tel./fax: +1 401 863 1418.
  E-mail address: William_Curtin@brown.edu (W.A. Curtin).

dislocation density, the study shows that the theory can quantitatively predict the stress–strain behavior and steady-state SRS of Al–Mg alloys as a function of strain rate, plastic strain, temperature and solute concentration. Comparisons with experimental data on Al–Mg alloys show broad quantitative agreement. The model also predicts the well-known but unexplained non-additivity of solute strengthening and forest hardening at low strain rates [13,14], the origin of which lies in the dynamic strengthening of the forest dislocations. And, the model predicts the transient behavior observed in strain–jump tests, which differs from the canonical behavior and is shown to arise from a combination of aging of the solute strengthening, with a fast transient, and aging of the forest strengthening, with a slower and asymmetric transient. The totality of predictions of the model suggests that the work here represents a major step forward in the understanding and predictability of dynamic strain aging in solute-strengthened materials.

2. The constitutive model

2.1. Mobile and forest strengthening and aging

According to the rate-dependent theory described in a companion paper, the general constitutive equation relating the strain rate to the stress and time history for plastic flow due to pinning of dislocations, and including aging phenomena that can occur during the time of pinning, depends on the instantaneous rate of escape of a dislocation from its local pinning points, given by

$$v(\tau(t), t, t_p) = v_0 \exp(-\Delta E(\tau(t), t, t_p)) \tag{1a}$$

Here, v_0 is a microscopic attempt frequency, and ΔE is the energy barrier controlling thermally activated dislocation motion, which depends on the resolved shear stress $\tau(t)$ acting on the dislocation at the current time t and on the time t_p at which the dislocation became pinned at the current obstacle. The above expression is normally applied to a single strengthening mechanism with some characteristic energy barrier, e.g. the barrier created by random solute configurations that pin the dislocation and give rise to the solute strengthening effect. The fundamental rate of escape in Eq. (1a) leads to a (plastic) strain-rate/stress-history constitutive relationship of the form

$$\dot{\varepsilon}(t) = \int_0^t \dot{\varepsilon}(t_p) v(\tau(t), t, t_p) \exp\left(-\int_{t_p}^t v(\tau(t'), t', t_p) \mathrm{d}t'\right) \mathrm{d}t_p \tag{1b}$$

for a test that begins at time $t = 0$ (i.e. $\dot{\varepsilon}(t) = 0$ $t < 0$). Eq. (1b) is the time derivative of

$$\Omega = \int_0^t \dot{\varepsilon}(t_p) \exp\left(-\int_{t_p}^t v(\tau(t'), t', t_p) \mathrm{d}t'\right) \mathrm{d}t_p \tag{1c}$$

where Ω is the elementary strain contributed by mobile dislocations jumping from one pinning point to the next, and is given by $\Omega = \rho_m b \rho_f^{-1/2}$ when the pinning is controlled by

forest dislocations. For complex loadings (e.g. strain-rate jump tests) Eq. (1b) coupled with Eq. (1c) is usually computationally more stable than Eq. (1b) alone. In the absence of any aging effects, Eq. (1b) reduces to the standard form $\dot{\varepsilon}(\tau(t)) = \dot{\varepsilon}_0 \exp(-\Delta E(\tau(t)))$ with some positive SRS. In the presence of aging, it is shown, as Hähner did in a much earlier set of papers [15,16], that nSRS cannot be achieved by any aging mechanism. The origin of this result is relatively simple: it is not possible to decrease the rate of thermal activation by increasing the applied stress. Based on this result, it is concluded that the nSRS clearly observed in many real materials must arise from an indirect aging effect, i.e. there is another aging process that does not occur directly on the mobile dislocations but does influence their motion.

The above realization leads one to consider multiple strengthening mechanisms. The extension of the energy barrier concept to multiple types of barriers is not clear, owing to possible interactions between the mechanisms, and various approximate methods have been proposed [14]. However, a simple one-dimensional model in which the mobile dislocation encounters energy barriers on two length scales, small and large, elucidates the basic physics. Consider an energy landscape for the dislocation as a function of glide position x of the form $E(x) = \Delta E_1 \sin(2\pi x/\ell_1) + \Delta E_2 \sin(2\pi x/\ell_2)$, corresponding to two different strengthening mechanisms with barriers and length scales (ΔE_1, ℓ_1) and (ΔE_2, ℓ_2), respectively. When a stress τ is applied, the total energy becomes $E(x) - \tau b \xi$, where b is the dislocation Burgers vector, and ξ is the lateral length of the dislocation segment. Taken separately, the zero-temperature strengths of the two mechanisms would scale as $\tau_1 \sim \Delta E_1/b\xi\ell_1$ and $\tau_2 \sim \Delta E_2/b\xi\ell_2$. Acting together, if the two scales are relatively different ($\ell_2 \gg \ell_1$), it is easy to show that the thermally activated motion is controlled by the smaller-scale mechanism 1 but with an effective applied stress of $\tau - \tau_2$, i.e. the second mechanism effectively acts as a backstress. This result is independent of the magnitudes of the strengths τ_1 and τ_2.

Applying the idea of multiple mechanisms to the present problem, the two mechanisms of (i) solute strengthening, the barriers for which occurs on scales of $\ell_1 \approx 1$ nm [17] and (ii) forest strengthening, the barriers for which are controlled by junctions on bow-out scales of $\ell_2 \approx 100$–1000 nm are considered. The combination of solute and forest strengthening mechanisms in various solid-solution alloys is well established, although rate theories are not often considered. Based on the discussion above, It is then assumed that the rate dependence is controlled by the solute strengthening of mobile dislocations, and that the forest dislocations exert a backstress that acts to restrain the mobile dislocations. The multidimensional aspect interaction of the two mechanisms is neglected, i.e. the actual junction formation/annihilation of a bowing mobile dislocation segment pinned by forests in the presence of an underlying stochastic solute pinning field. Approximate analyses suggest, however, that the forests do act to generate backstresses on the mobiles and thus that the result

emerging from the simple one-dimensional model is accurate. More importantly, aging effects of both the mobile and forest dislocations are included, which give rise to time-dependence of both strengthening mechanisms. In this framework, the rate-dependence for dislocation escape is given by

$$v(\tau, t, t_p) = v_0 \exp(-\Delta E(\tau(t, t_{af}, \varepsilon), t, t_p)) \qquad (2)$$

where the energy barrier $\Delta E(\tau, t, t_p)$ is that for solute strengthening with time-dependent diffusion but with a stress dependence that accounts for the rate dependence and aging of the forests through a contribution $\Delta \tau_f(t, t_{af}, \varepsilon)$ that is the time-dependent backstress exerted by the forest dislocations and is a function of the current time, the current strain (which determines the forest spacing, and hence the junction strength), and the aging time of the forests t_{af}. In the absence of any forest aging, $\Delta \tau_f(t, t_{af}, \varepsilon)$ reduces to the static forest strengthening contribution.

The key point within the above framework is that the forest aging times are disconnected from the aging times of the mobiles. That is, there is no relationship between the time at which a particular mobile dislocation becomes pinned t_p and the aging time(s) of any of the forest dislocations t_{af}. The forest dislocations are formed at various times in the strain history and begin aging. Subsequently, at completely independent later times $\{t_p\}$, various mobile dislocations intersect these forests and become pinned, after which aging of each mobile occurs over the subsequent time $t - t_p$. In the formulation for the strain rate given by Eq. (1b), this means that the entire term $\Delta \tau_f(t, t_{af}, \varepsilon)$ appearing in the integral within the exponential is independent of the integration variable t', which is the mobile dislocation pinning time. Therefore, the overall rate dependence is modified solely through the addition of the backstress $\Delta \tau_f(t, t_{af}, \varepsilon)$. This backstress itself shows negative strain rate sensitivity because the strengths of the forests increase as the aging time increases, and the aging time of the forests is inversely proportional to the applied strain rate. Thus, overall nSRS will emerge from the positive (but reduced) SRS of the mobile aging and the nSRS due to the forest aging.

The paper now turns to an explicit model for the energy barrier $\Delta E(\tau, t, t_p)$, which is the energy barrier for thermal activation of dislocations out of pinning points caused by stochastic fluctuations in the solute atom distribution, modified by aging via solute diffusion to both mobile and forest dislocations. The general form for the energy barrier is

$$\Delta E(\tau, t, t_p) = \frac{\Delta E_0}{kT} \left(1 - \frac{\tau(t, t_{af}, \varepsilon, t_p)}{\tau_0}\right)^{\alpha} \qquad (3)$$

where ΔE_0 is the zero stress energy barrier, k is the Boltzmann constant, T is the absolute temperature, τ_0 is the zero-temperature flow stress due to static solute strengthening, and α is a parameter. Molecular dynamics simulations performed for 5XXX Al–Mg systems suggest $\alpha = 3/2$ [17], which also emerges from various analytic models of

dislocation energy or force profiles [14]. The stress $\tau(t, t_{af}, \varepsilon, t_p)$ is the time-dependent stress acting on the mobile dislocation during pinning. It has been shown previously that the aging of the mobile dislocations is properly represented by a time-dependent backstress-like term $\Delta \tau_m(t - t_p)$ during the pinning time $t - t_p$. Thus, the stress $\tau(t, t_{af}, \varepsilon, t_p)$ includes the resolved applied shear stress τ_{app}, the backstress due to forest hardening with aging $\Delta \tau_f(t, t_{af}, \varepsilon)$, and the contribution $\Delta \tau_m(t - t_p)$ from aging of the mobile dislocation during pinning time, so that

$$\tau(t, t_{af}, \varepsilon, t_p) = \tau_{app}(t) - \Delta \tau_m(t - t_p) - \Delta \tau_f(t, t_{af}, \varepsilon) \qquad (4)$$

Eqs. (1b), (2)–(4) give the general, formal structure of the constitutive model.

2.2. The aging mechanism

The aging mechanism for both mobile and forest dislocations is the diffusion of solutes toward the dislocation. The interaction between dislocations and solute atoms in solid solutions resulting in solute diffusion towards the dislocations cores has been studied for more than 50 years. Various mechanisms have been proposed associated with bulk or pipe diffusion, and acting on mobile dislocations or forest junctions [2–5,11,18–20]. However, quantitative evaluation of some of these models is difficult owing to either the existence of adjustable parameters or the absence of actual microscopic mechanisms. More importantly, in Al–Mg it has recently been noted that the bulk diffusion of Mg in Al at room temperature is far too slow, by a factor of 10^6, to account for the dynamic strain aging effects observed in experiments. Picu and Zhang [21] have further shown that pipe diffusion is also inadequate for accelerating the accumulation of solutes in the dislocation core, primarily owing to the absence of an energetic driving force for the diffusion. Another feature of these models is that, owing to the long-range nature of the dislocation strain field, a fully saturated "cloud" of solute atoms around a fixed dislocation corresponds to an infinite binding energy and infinite strengthening such that, if extensive diffusion were to occur, dislocations would be very strongly pinned and never escape at the stresses and rates typical of experiments.

A recent model has rectified all these issues by exposing the fact that single atomic jumps of solute atoms across the slip plane in the core of an Al edge dislocation have a high energetic driving force, owing to the high compression and tension on either side of the slip plane, and also a greatly reduced energy barrier for diffusion [10]. This "cross-core diffusion" model thus accounts for both the faster time scale and lower saturation energy and strength relative to the long-standing models. Predictions of the model, using only material parameter values obtained from atomistic simulations, showed good agreement with experiments in Al–Mg, further reinforcing the basic validity of the model. However, that model was not a full rate theory and, following the companion paper, the "cross-core" mechanism

acting on mobile dislocations alone cannot yield the nSRS seen experimentally.

Here, the cross-core diffusion model is applied to the strengthening of both mobile dislocations and forest dislocations. The mechanism of solute diffusion in the core of a dislocation is independent of whether the dislocation is actually mobile (pinned by some pre-existing static solute configuration) or forest (immobile because the resolved stresses are insufficient). Thus, the fundamental mechanism is identical to that of Curtin et al. [10], but its application to forest strengthening is made using a recent theory by Picu et al. [11,12].

In the cross-core diffusion model, diffusion of solutes across the core (e.g. from the compression to the tension side for solutes that are larger than the host lattice, as for Mg in Al) leads to an increasing binding energy of the dislocation to its current location. An analytic solution for the diffusion process yields the dislocation binding energy change per unit length of dislocation of the form

$$\Delta E^{\mathrm{core}}(t_{\mathrm{a}}) = \Delta E^{\mathrm{core}}_{\infty}\left(1 - \exp\left(-\left(\frac{t_{\mathrm{a}}}{t_{\mathrm{d}}}\right)^n\right)\right) \tag{5}$$

where t_{a} is the aging time, whether for forest or mobile dislocation. The time t_{d} is an intrinsic cross-core solute diffusion time, and $\Delta E^{\mathrm{core}}_{\infty}$ is a saturation energy value for the cross-core diffusion process, both given explicitly later. The parameter n is derived to be 1 when the migration enthalpy for diffusion is assumed uniform across the width of the atomistic core. For any distribution of migration enthalpies across the width of the core, values of $n < 1$ can be used to fit the full solution. To permit such latitude, in the absence of any available explicit calculations, values of $n = 1/3$ and $n = 1$ are considered here.

The strengthening of mobile dislocations once pinned has been derived directly from Eq. (5) for the case $n = 1$ by Curtin et al. [10], and is proportional to $\Delta E^{\mathrm{core}}(t - t_{\mathrm{p}})$. For $n < 1$, proportionality is not strictly true, and the analysis has not been carried through. For simplicity, direct proportionality is assumed for $n < 1$, so that the additional strength of a mobile dislocation pinned at time t_{p} is

$$\Delta \tau_{\mathrm{m}}(t - t_{\mathrm{p}}) = \Delta \tau_{\mathrm{m}\infty}\left(1 - \exp\left(-\left(\frac{t - t_{\mathrm{p}}}{t_{\mathrm{d}}}\right)^n\right)\right)$$
$$\propto \Delta E^{\mathrm{core}}(t - t_{\mathrm{p}}) \tag{6}$$

where the saturation strength $\Delta \tau_{\mathrm{m}\infty}$ is related to $\Delta E^{\mathrm{core}}_{\infty}$ and other material parameters (e.g. the inter-atomic and dislocation segment lengths, solute concentration and temperature) as described below. It will be kept in mind that the role of n in Eq. (6) is less important to the macroscopic results than is its role in Eq. (5).

The strengthening of mobile dislocations by forest dislocations is well understood theoretically, numerically and experimentally [2,6–8,22–28]. The strengthening arises from the formation of dislocation junctions, and strain hardening ensues from dislocation multiplication. The role of junctions in influencing SRS is recognized in the Cott-

rell–Stokes law, and their role in nSRS was proposed in qualitative models by Kocks [13,29]. In a major recent advance, Picu and colleagues [11,12] identified the role of aging phenomena in the strength of junctions. Aging of a forest dislocation via diffusion of solutes binds the forest dislocation to its current configuration. When a mobile dislocation arrives to form a junction, the formation of the junction is inhibited by the necessity of peeling the aged forest dislocation out of its favorable local position. This leads to shorter junction segments, as a function of the extra binding energy of the forest owing to aging, and then to a higher junction strength, because bowing of the forests is restricted. A mesoscopic analysis of dislocation junction formation and failure in face-centered cubic (fcc) materials yields a forest strengthening as a function of both forest density, as usual, and an additional binding energy of the forests [12]. For an additional binding energy per unit length that is small in comparison with the fundamental dislocation line energy A, i.e. $\Delta E^{\mathrm{core}}_{\infty}/A \approx 0.05$ or smaller, the forest strengthening is

$$\Delta \tau_{\mathrm{f}}(t_{\mathrm{af}}) = \bar{\tau}_{\mathrm{f}}\left(1 + 8.7\frac{\Delta E^{\mathrm{core}}(t_{\mathrm{af}})}{A}\right)$$
$$\equiv \bar{\tau}_{\mathrm{f}}\left[1 + \delta\left(1 - \exp\left(-\left(\frac{t_{\mathrm{af}}}{t_{\mathrm{d}}}\right)^n\right)\right)\right] \tag{7}$$

where $A = \frac{3Gb^2}{4\pi(1-v)}$ is the line tension energy per unit length of dislocation, G is the shear modulus ($G = 29573.3 - 14\mathrm{T(K)}$ MPa), and v is the Poisson ratio. In Eq. (7), $\bar{\tau}_{\mathrm{f}} = 1.37A\sqrt{\rho_{\mathrm{f}}}/b$ is exactly the usual forest hardening contribution without aging, where ρ_{f} is the density of the forest dislocations and depends directly on the plastic strain. The forest aging-strengthening factor $\delta = 8.7\Delta E^{\mathrm{core}}_{\infty}/A$ is introduced for later reference. Eq. (7) is an average over the strengths of all possible types of fcc dislocation junctions with significant strengths (Lomer Cottrell lock, glissile junction and junctions with parallel Burgers vectors). For Al at room temperature, values of the relevant material parameters are $v = 0.347$, $b = 2.851$ Å, $G \cong 25.3$ GPa and $A \cong 0.47$ eV/Å.

Since the aging times of the forest dislocations are not directly connected with the aging times of the mobiles that form junctions with the forests, the detailed distribution of forest aging times is not particularly important. As a lowest-order approximation, this study thus follows Picu et al. and takes an average forest aging time given by

$$t_{\mathrm{af}}(t) = \frac{\int_0^t (t - t')\frac{\mathrm{d}\rho_{\mathrm{f}}}{\mathrm{d}t'}\mathrm{d}t'}{\int_0^t \frac{\mathrm{d}\rho_{\mathrm{f}}}{\mathrm{d}t'}\mathrm{d}t'} \tag{8}$$

where Eq. (8) recognizes the fact that the formation of forest dislocation density is time dependent and related to the total plastic strain in the material.

Eqs. (6)–(8) summarize the strengthening contributions due to aging of both mobile and forest dislocations and due to evolution of the forest dislocation density. Note that all of the aging phenomena stem from the cross-core mechanism and the resulting energy vs. time given in

Eq. (5) with subsequent results being a natural consequence of the influence of this aging mechanism on the strengths vs. time. Furthermore, the functional forms of both aging terms in Eqs. (6) and (7) are derived to be in exactly the form assumed in many literature models, i.e. $\Delta\tau(t_a) = \Delta\tau_\infty(1 - \exp(-(\frac{t_a}{t_d})^n))$, but now placed on a firm mechanistic basis with parameters determined from atomistic and mesoscale material properties.

The complete constitutive model proposed in this paper is thus represented by the fundamental rate theory Eq. (1b) or (1c), the basic form of the energy barrier Eq. (3), the effective stress in Eq. (4) and the time-dependent and strain-dependent contributions to the effective stress given by Eqs. (6) and (7), as derived from Eq. (5). Below, the detailed microscopic expressions for the various constants (Section 2.3) and the evolution of the forest density with plastic strain (Section 2.4) are shown.

2.3. Material parameters

In the preceding sections, the underlying dependences of various energies, energy barriers and strengths on material parameters have been suppressed. Here, all the relevant relationships are presented, so that the theory is shown clearly and completely to connect macroscopic deformation to microscopic material parameters.

Dimensional analysis described by Labusch [30] and Zaiser [31], and supported by the recent results of Olmsted et al. [17], indicate that the zero temperature energy barrier associated with solute strengthening by a random distribution of static solute atoms scales is

$$\Delta E_0 = \Lambda \left(\frac{A w^4 \hat{U}^2 c}{b^3} \right)^{1/3} \tag{9}$$

while the corresponding zero temperature strength stress energy is

$$\tau_0 = \tau_P + \frac{3\Lambda}{2} \left(\frac{\sqrt{2}\hat{U}^4 c^2}{Aw} \right)^{1/3} \frac{1}{b^3} \tag{10}$$

where $\tau_P \cong 3$ MPa is the Peierls stress, c is the solute concentration in per cent, $\hat{U}$ is a characteristic interaction energy between a single solute and a straight dislocation, w is a characteristic range for the interaction, and Λ is an adjustable scaling factor. For Al–Mg, Olmsted et al. have found $\hat{U} \cong 0.1$ eV and $w \cong 20$ Å. $\Lambda \approx 2$ yields a strength of $\tau_0 = 70$ MPa at $c = 5\%$, consistent with experimental data on initial yield strengths at near-zero plastic strain.

Molecular statics simulations coupled with analytical methods [10] show that the saturation binding energy per unit length in cross-core diffusion is

$$\Delta E_\infty^{\text{core}} = \frac{2c\bar{w}}{\sqrt{3}b^2} \overline{\Delta W} \tanh\left(\frac{\overline{\Delta W}}{2kT}\right) \tag{11}$$

where $\overline{\Delta W}$ is the average differential binding energy between atomic sites on either side of the slip plane within the (dissociated) core of width $\bar{w}$. For Al–Mg alloys, atomistic

simulations show $\overline{\Delta W} \cong 0.13 \pm 0.05$ eV with $\bar{w} \approx 7.5b = 21$ Å. At room temperature, this yields a maximum binding energy per unit length of $\Delta E_\infty^{\text{core}} \cong 0.0040$ eV/Å for each 1% of Mg solute.

The intrinsic diffusion time is associated with the average activation enthalpy for cross-core diffusion, ΔH_c, and the energy difference $\overline{\Delta W}$ across the slip plane. For Mg in Al, diffusion from compression to tension (favorable) is controlled by the enthalpy $\Delta H_c - \overline{\Delta W}/2$, and diffusion from tension to compression (unfavorable) is controlled by the enthalpy $\Delta H_c + \overline{\Delta W}/2$. The appropriate time scale for the diffusion process is thus given by

$$t_d = \frac{1}{3v_0} \exp\left(\frac{\Delta H_c - \overline{\Delta W}/2}{kT}\right) \tag{12}$$

where v_0 is the attempt frequency for atomic motion. For Al–Mg, $v_0 = 3.8 \times 10^{13}$ s^{-1} is consistent with the rates for bulk Mg diffusion, and atomistic models yield $\Delta H_c = 0.97$ eV for several barriers near the cores of the partial dislocations making up the dissociated dislocation. Since the activation enthalpy for the bulk Mg diffusion in Al is $\sim$1.2 eV, the cross-core process is saturated (reaches its limiting values) on times that are still extremely small on the time scale associated with bulk diffusion and traditional solute cloud formation, and such processes are therefore neglected.

The strength associated with aging of the mobile dislocations by solutes is given by

$$\Delta\tau_m(t - t_p) = \alpha\Delta E^{\text{core}}(t - t_p)/\bar{w}b \tag{13}$$

where $\alpha \approx 0.56$ is a coefficient accounting for the energy variation along the core obtained from atomistic studies on Al–Mg. The maximum mobile strengthening is then

$$\Delta\tau_{m\infty} = \alpha\frac{2c}{\sqrt{3}b^3} \overline{\Delta W} \tanh\left(\frac{\overline{\Delta W}}{2kT}\right) \tag{14}$$

At room temperature and $c = 5\%$, $\Delta\tau_{m\infty} \cong 28.69$ MPa.

Using the saturation cross-core diffusion binding energy of Eq. (11) in Eq. (7) yields the saturated forest aging strengthening of

$$\Delta\tau_{f\infty} = \bar{\tau}_f \left(1 + 8.7\frac{2c\bar{w}}{\sqrt{3}b^2} \frac{\overline{\Delta W}}{A} \tanh\left(\frac{\overline{\Delta W}}{2kT}\right) \right) \tag{15}$$

The above equations complete the description of the constitutive model, demonstrating that every quantity is connected directly to independently determined quantities and experimentally controlled variables such as solute concentration and temperature. Eqs. (9) and (10) are only scaling relations, and so precise calculations cannot be made. However, the estimates are consistent with molecular dynamics studies and the scaling with, for instance, solute concentration, is a testable relationship.

2.4. Dislocation density evolution and calibration

The constitutive theory above does not address the evolution of the forest dislocation density with strain. This

evolution is, however, considered to be completely independent of the aging mechanisms or strengthening mechanisms. There are a number of theories for the evolution of the mobile and forest dislocations in terms of nucleation, reaction and annihilation rates [7,8,24,27,28], but their net result is primarily a forest dislocation density vs. strain. Rather than using such equations, which then involves selecting values for microscopic parameters for nucleation and annihilation that must be calibrated against experiments anyway, the forest density evolution is modeled phenomenologically, as in earlier works [6,11,22,29]. Specifically, it is assumed that the forest density vs. strain follows the general form

$$\rho_f = \rho_f^{sat}(1 - \exp(-(\varepsilon/\bar{\varepsilon})^p)) \tag{16}$$

where the parameters ρ_f^{sat}, $\bar{\varepsilon}$ and p are chosen appropriately, as described below. The average aging time of the forests, Eq. (8), can then be recast in terms of the strain as

$$t_{af}(\varepsilon) = \frac{\int_0^\varepsilon \frac{1}{\dot{\varepsilon}}\rho_f(\varepsilon')d\varepsilon'}{\rho_f(\varepsilon)} \tag{17}$$

The variation in forest dislocation density with strain imposes a strain dependence on the elementary strain through the relationship $\Omega(\varepsilon) = \rho_m b \rho_f^{-1/2}$. Assuming that the dependence of the mobile dislocation density on the strain is proportional to the forest dislocation density but four times smaller, as emerges from more complex models, the elementary strain is $\Omega = b/4[\rho_f^{sat}(1 - \exp(-(\varepsilon/\bar{\varepsilon})^p))]^{1/2}$. More accurate estimations for Ω can be made, but most results are relatively insensitive to Ω.

To minimize parameters that are largely unimportant for showcasing the predictions of the model, it is assumed that single values of $\bar{\varepsilon}$ and p are relevant to all Al–5XXX aluminum alloys studied here at all temperatures, independent of other alloy additions beyond Mg. Thus, it is envisioned that only the parameter ρ_f^{sat} differs between materials and with temperature. It is then recognized that the stress–strain behavior at sufficiently low temperatures and/or high strain rates is completely devoid of any aging effects, because the rate of cross-core solute diffusion is too slow to make any contributions to the deformation behavior. Thus, one can determine the parameters ρ_f^{sat}, $\bar{\varepsilon}$ and p independently of any aging effects by fitting to stress–strain data obtained at either low temperature or high strain rate. In the low-temperature regime, the theory reduces simply to a sum of solute strengthening and forest strengthening contributions as

$$\dot{\varepsilon} = v_0\Omega\exp\left(-\frac{\Delta E_0}{kT}\left(1 - \frac{\tau - \bar{\tau}_f(\varepsilon)}{\tau_0}\right)^\alpha\right) \tag{18}$$

which can be inverted to yield

$$\tau = \tau_0 - \tau_0\left(\frac{kT}{\Delta E_0}\ln\left(\frac{\dot{\varepsilon}}{v_0\Omega}\right)\right)^{\frac{1}{\alpha}} + \bar{\tau}_f(\varepsilon) \tag{19}$$

The first term is the zero-temperature solute strength, the second term is the rate- and temperature-dependent decrease in solute strengthening, and the third term is the

forest strengthening term that provides strain hardening. These results are in terms of the resolved shear stress acting along the glide plane of the dislocation (i.e. the Peach–Koehler force). σ measured in simple tension tests of untextured polycrystals is connected to the stress, using the Taylor relation

$$\sigma = M\tau \quad M = 3 \tag{20}$$

The parameters ρ_f^{sat}, $\bar{\varepsilon}$ and p, and the scaling parameter Λ from Eqs. (9 and 10) are then determined by fitting the model (Eq. (19)) to the experimental stress–strain curves outside the aging regime for various Al–Mg alloys. For the experiments reported by Benallal and collaborators [32] on AA5083-H116 (4.5–4.9%Mg, 0.7%Mn, 0.14%Cr) at a high strain rate $\dot{\varepsilon} = 1.31 \cdot 10^3$ s^{-1} and room temperature, one obtains

$$\rho_f^{sat} \approx 12.78 \cdot 10^{14} \text{ m}^{-2}; \quad p = 1.15;$$
$$\bar{\varepsilon} = 0.26; \quad \text{and} \quad \Lambda = 2.07 \tag{21}$$

The corresponding stress–strain curve is shown in Fig. 1. For the experiments performed by Picu et al. [33] on AA5182-O (4.5%Mg, 0.2–0.5%Mn, 0.15%Cu, 0.25%Zn, 0.2%Si, 0.1%Ti, 0.35%Fe) at low temperature $T = -120$ °C and $\dot{\varepsilon} = 10^{-3}$/s, one obtains

$$\rho_f^{sat} \approx 7.73 \cdot 10^{14} \text{ m}^{-2}; \quad p = 1.15;$$
$$\bar{\varepsilon} = 0.26; \quad \text{and} \quad \Lambda = 2.07 \tag{22}$$

where only the saturation value of the forest dislocation density differs from the previous case. The corresponding stress–strain curves are also shown in Fig. 1. The full model,
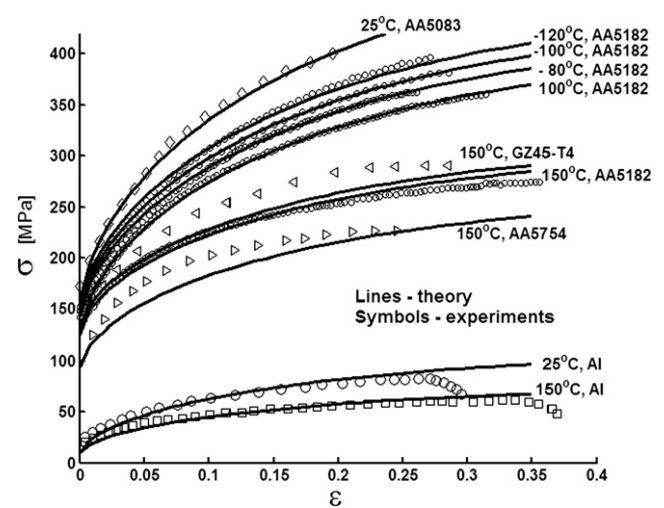

Fig. 1. Tensile stress–strain curves for various Al–5XXX alloys outside the domain of nSRS (low temperature, high rate or high temperature), as measured and predicted by the present model, with the dislocation density evolution parameters used as adjustable quantities to fit the experiments. Lines: predictions; Symbols: experiments. Strain rates are $\dot{\varepsilon} = 1.3 \cdot 10^3$/s for AA5083-H11 (4.7%Mg) [32] ; $\dot{\varepsilon} = 10^{-3}$/s for AA5182-O (4.5%Mg) [33]; $\dot{\varepsilon} = 10^{-3}$/s for GZ45-T4 (4.5%Mg), AA5754 (3.1%Mg) [34] and pure Al [35]. Dislocation density evolution parameters are obtained as $p = 1.15$, $\bar{\varepsilon} = 0.26$ and varying, ρ_f^{sat} with the solute strengthening prefactor $\Lambda = 2.07$, as shown in Table 1.

with atomistically derived parameters, as presented in the next section, predicts that these materials are, under the above conditions, outside the nSRS domain so that any subsequent results have not been biased by fitting.

One can also calibrate to high temperature material response. This regime is complicated by the aging by solute diffusion, but also by the fact that the forest dislocation density decreases owing to annihilation and other recovery mechanisms that are outside the scope of the present theory. However, at high temperatures and moderate to slow strain rates, aging by cross-core solute diffusion is fully saturated, because it occurs very fast compared with the loading rates. In this regime, the strain-rate/stress behavior is

$$\dot{\varepsilon} = v_0 \Omega \exp\left(-\frac{\Delta E_0}{kT}\left(1 - \frac{\tau - \Delta\tau_{m\infty} - \bar{\tau}_f(\varepsilon)(1+\delta)}{\tau_0}\right)^\alpha\right) \quad (23)$$

or

$$\tau = \tau_0 + \Delta\tau_{m\infty} - \tau_0\left(\frac{kT}{\Delta E_0}\ln\left(\frac{\dot{\varepsilon}}{v_0\Omega}\right)\right)^{\frac{1}{\alpha}} + \bar{\tau}_f(\varepsilon)(1+\delta) \quad (24)$$

In comparison with Eq. (19), Eq. (24) contains an additional strength due to strengthening of the mobile dislocations and an additional forest strengthening/hardening contribution that scales with forest dislocation density. With the temperature dependence of these terms given in Eqs. (7), (14), and (15), Eq. (26) is the predicted high-temperature stress–strain curve. Keeping $\bar{\varepsilon}$, p and Λ as given by Eq. (22), Eq. (24) is fit to high temperature data on AA5182-O at $\dot{\varepsilon} = 10^{-3}/\text{s}$ to yield saturation densities

$$\rho_f^{sat} \approx 4.94 \cdot 10^{14} \text{ m}^{-2} \quad T = 100\,^\circ\text{C}$$
$$\rho_f^{sat} \approx 2.19 \cdot 10^{14} \text{ m}^{-2} \quad T = 150\,^\circ\text{C} \quad (25)$$

and the stress–strain curves shown in Fig. 1. As expected, the saturation density begins to decrease rapidly at elevated temperatures. For later predictions at intermediate temperatures, one linearly interpolates between the forest dislocation saturation values at $-120\,^\circ\text{C}$ and $100\,^\circ\text{C}$ and between the values at $100\,^\circ\text{C}$ and $150\,^\circ\text{C}$ (i.e. bilinear interpolation). The predictions of the stress–strain curve at $T = -100\,^\circ\text{C}$ and $T = -80\,^\circ\text{C}$, still in a regime where aging effects are negligible, are shown in Fig. 1, and the agreement is excellent.

The exact same values of $\bar{\varepsilon}$, p, ρ_f^{sat} and Λ in Eqs. (22) and (25) were also used for two other Al alloys, AA5754-O (3.1%Mg, 0.5%Mn, 0.3%Cr, 0.15%Zn, 0.1%Cu, 0.4%Si) and AAGZ45-T4 (4.5%Mg, 1.5%Zn, 0.38%Cu, 0.09%Si) [34], at different temperatures. The experimental and predicted stress–strain curves at $T = 150\,^\circ\text{C}$ are shown in Fig. 1, and good agreement is again obtained without any fitting.

Finally, the data of Ayres [35] on pure Al and binary Al–Mg systems are considered. For pure Al, there is no solute strengthening and no aging, and so the forest density parameters can be found directly. Keeping the parameters $\bar{\varepsilon} = 0.26$ and $p = 1.15$ fixed, the pure Al data at $\dot{\varepsilon} = 2.9 \cdot 10^{-3}/\text{s}$ yield

$$\rho_f^{sat} \approx 0.96 \cdot 10^{14} \text{ m}^{-2} \text{ for } T = 25\,^\circ\text{C}$$
$$\rho_f^{sat} \approx 0.49 \cdot 10^{14} \text{ m}^{-2} \text{ for } T = 150\,^\circ\text{C} \quad (26)$$

The experiments and predictions are also shown in Fig. 1. For the Al–Mg binary alloys, a slightly lower value of the parameter $\Lambda = 1.87$ was needed to fit Al–3%Mg [35] at $T = 150\,^\circ\text{C}$ and $\dot{\varepsilon} = 2.9 \cdot 10^{-3}/\text{s}$ while maintaining $\rho_f^{sat} \approx 0.49 \cdot 10^{14} \text{ m}^{-2}$; this fit will be shown later along with other experiments and predictions (see Fig. 7). The lower Λ value is qualitatively consistent with the fact that, in fitting $\Lambda = 2.07$ to the commercial alloys, the strengthening due to the secondary alloying elements that are absent in the binary alloy have been indirectly included.

Table 1 presents all the parameters fitted in the model. Excellent agreement is obtained using the fixed values $\bar{\varepsilon} = 0.26$, $p = 1.15$, for all the materials. The saturation value of the forest dislocation ρ_f^{sat} must vary significantly among materials, which may be associated with different processing methods for different materials and with some unknown influence of alloying on dislocation evolution. The scaling parameter $\Lambda = 1.87$ for binary alloy and $\Lambda = 2.07$ for the commercial materials. It is emphasized that none of the parameters calibrated using experimental data is directly connected to dynamic strain aging, and the parameters are determined under conditions where dynamic strain aging is absent – aging is either completed or it does not have enough time to occur. All other parameters characterizing the strength associated with aging (the binding energy for the solute atoms to the dislocation cores, the cross-core diffusion time parameter, the maximum additional strength of mobile and forest dislocations due to the presence of solutes) are obtained from independent studies at the nano and meso scales [10–12].

3. Predictions

It is now demonstrated that the constitutive model quantitatively predicts all the trends observed in the SRS of Al–Mg alloys with no adjustable parameters. Specifically, successive sections study the steady-state SRS vs. plastic strain, temperature and solute concentration. This spectrum of results represents various "cuts" through the parameter space of the full constitutive law, and is thus a subset of the full scope of possible results. Then non-steady-state strain-rate-jump tests and non-additivity of solute and forest strengthening due to aging phenomena are examined.

Before proceeding, note that an accurate analytic approximation for the constitutive model under steady-state conditions can be derived following a procedure discussed in Appendix 1 of the companion paper, and is presented in Appendix 1 of this paper. The error in the predicted stress due to the approximation made to obtain an analytic result is <4% and is entirely contained within the representation of the mobile aging contribution. Thus, while the integral form of Eq. (1b), with all the mechanistically based inputs, is rather daunting, a single formula

Table 1
Parameters calibrated by experiments outside the nSRS domain

Parameter	Reference	Material	Testing conditions	Numerical value
Λ Zero temperature flow stress scaling coefficient	[32]	AA 5083 (c = 4.6%)	$T = 25\ ^{\circ}C$, $\dot{\varepsilon} = 1.3 \cdot 10^3\ s^{-1}$	2.07
	[33]	AA 5182 (c = 4.5%)	Not fitted	Same as AA5182
	[34]	AA5754-O (c = 3.1%)	Not fitted	Same as AA5182
	[34]	GZ45-T4 (c = 4.5%)	Not fitted	Same as AA5182
	[35]	Binary Al–Mg (c = 3%)	$T = 150\ ^{\circ}C$, $\dot{\varepsilon} = 3 \cdot 10^{-3}\ s^{-1}$	1.87
ρ_f^{sat} Saturation forest dislocation density	[32]	AA 5083	$T = 25\ ^{\circ}C$, $\dot{\varepsilon} = 1.3 \cdot 10^3\ s^{-1}$	$12.78 \cdot 10^{14}\ m^{-2}$
	[33]	AA5182	$T = -120\ ^{\circ}C$, $\dot{\varepsilon} = 10^{-3}\ s^{-1}$ $T = 100\ ^{\circ}C$, $\dot{\varepsilon} = 10^{-3}\ s^{-1}$ $T = 150\ ^{\circ}C$, $\dot{\varepsilon} = 10^{-3}\ s^{-1}$	$7.73 \cdot 10^{14}\ m^{-2}$ $4.94 \cdot 10^{14}\ m^{-2}$ $2.19 \cdot 10^{14}\ m^{-2}$
	[34]	AA5754	Not fitted	Same as AA5182
	[34]	GZ45-T4	Not fitted	Same as AA5182
	[35]	Pure Al	$T = 25\ ^{\circ}C$, $\dot{\varepsilon} = 3 \cdot 10^{-3}\ s^{-1}$ $T = 150\ ^{\circ}C$, $\dot{\varepsilon} = 3 \cdot 10^{-3}\ s^{-1}$	$0.96 \cdot 10^{14}\ m^{-2}$ $0.46 \cdot 10^{14}\ m^{-2}$
p Exponent for forest dislocation density evolution	[32–35]	All materials	Fitted for AA5182 $T = -120\ ^{\circ}C$, $\dot{\varepsilon} = 10^{-3}\ s^{-1}$	1.15
$\bar{\varepsilon}$ Reference strain for forest dislocation density evolution	[32–35]	All materials	Fitted for AA5182 $T = -120\ ^{\circ}C$, $\dot{\varepsilon} = 10^{-3}\ s^{-1}$	0.26

can be written down that captures the full scope of steady-state phenomena.

3.1. Steady-state SRS

Fig. 2a shows the tensile flow stress vs. steady-state strain rate as predicted by the model for an Al–4.6%Mg alloy at 5% deformation and room temperature for $n = 1$ and $n = 1/3$. Also shown are experimental data reported by Benallal et al. [32] for Al–Mg alloy 5083-H116. Fig. 2b shows the corresponding predictions for the SRS $m = d(\log \tau)/d(\log \dot{\varepsilon})$. Negative SRS is observed experimentally in the approximate range $5 \cdot 10^{-4}$–$10^0\ s^{-1}$, and the model predicts nSRS over a comparable range. In addition, the magnitude of the stress decrease is relatively comparable with the experiments. The theory predicts that at strain rates $>10^{-1}$–$10^0\ s^{-1}$, thermal escape occurs too quickly for the solute diffusion to occur, so that the results fall on the "no-aging" curve given by Eq. (19). At very small strain rates, both mobile and forest dislocations are completely aged, and the stress–strain curves follow the "high-temperature/low-strain-rate" limit of Eq. (24), which was used to fit the forest dislocation parameters. In the small strain-rate regime, the magnitude of the aging strength of mobile dislocations $\Delta\tau_{m\infty}$ predicted by the model ($\Delta\tau_{m\infty}/\tau_o = 0.376$) suppresses the

strain-rate dependence over a very wide range, leading to a nearly constant stress vs. strain rate, and thus a very small positive SRS. To elucidate the role of this parameter, Fig. 2 also shows predictions for no mobile aging ($\Delta\tau_{m\infty}/\tau_o = 0$) and an intermediate value ($\Delta\tau_{m\infty}/\tau_o = 0.188$). These results clearly show that $\Delta\tau_{m\infty}$ only plays a major role at low strain rates and that most of the nSRS regime is controlled by the forest aging. The remainder of this paper uses the computed value $\Delta\tau_{m\infty}/\tau_o = 0.376$, recognizing that such a high value will influence detailed predictions primarily at low strain rates or high temperatures.

The value of n has an effect on the magnitude of the stresses and the width of the nSRS regime. For $n = 1$, the nSRS regime is relatively narrow with a large stress drop, whereas for $n = 1/3$ the range of nSRS is broadened out, but the stress drop is smaller. The main role of n is in the forest aging term, Eq. (7), rather than the mobile aging term. Recall that $n < 1$ for the core energy change, and the forest aging mechanism is expected for any modest spread in the diffusion activation enthalpies across the core region. Thus, results for $n = 1/3$ are justifiable and most likely correspond to realistic materials [3,7,15,36,37] compared with the more stringent but analytically convenient $n = 1$.

Fig. 3a shows the flow stress vs. strain rate for various levels of plastic strain and Fig. 3b shows the corresponding
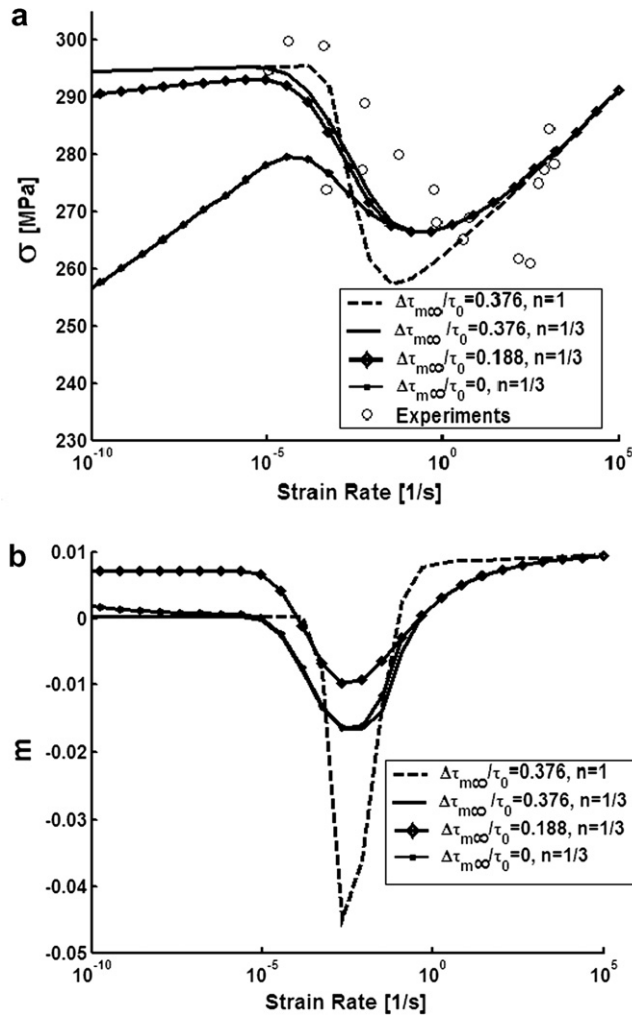
Fig. 2. (a) Tensile flow stress vs. applied steady-state strain rate, at 5% deformation and room temperature. Lines: model predictions, with variations in some quantities to elucidate some dependences. Symbols: experiments for Al5083-A116 [32]. (b) SRS parameter $m = \mathrm{d}(\log \tau)/\mathrm{d}(\log \dot{\varepsilon})$ corresponding to the predictions shown in (a). In both (a) and (b), variations in the mobile solute aging parameter $\Delta\tau_{\mathrm{m}\infty}$ are shown only to highlight the regimes where this parameter plays a significant role.
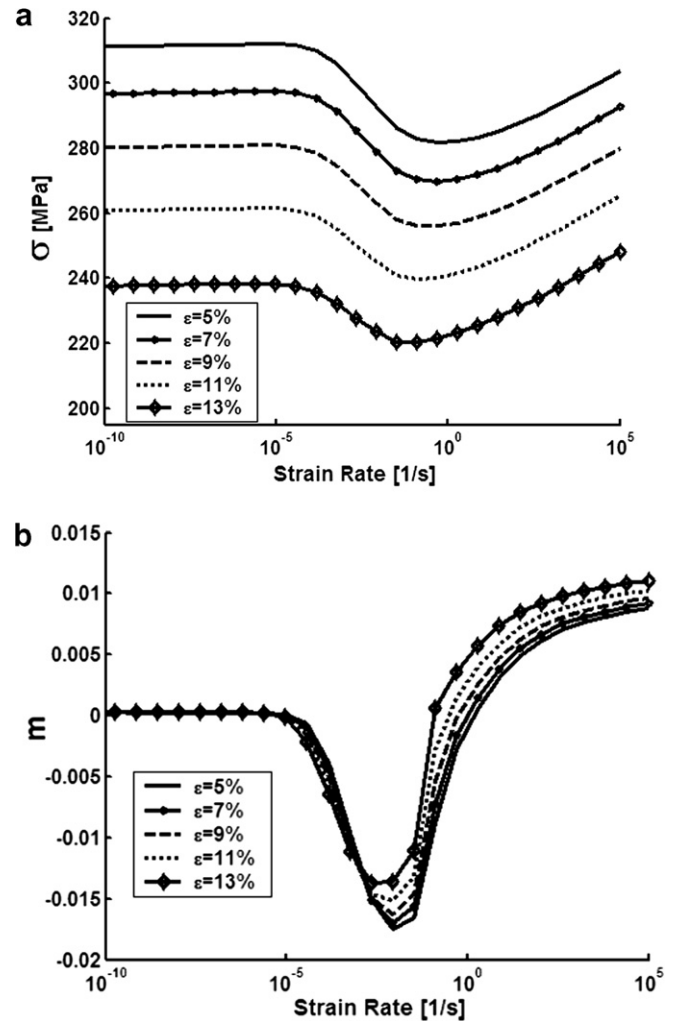

Fig. 3. (a) Tensile flow stress vs. strain rate, for various plastic strains at room temperature for AA5182 (with $n = 1/3$). (b) Strain-rate sensitivity parameter $m = \mathrm{d}(\log \tau)/\mathrm{d}(\log \dot{\varepsilon})$ corresponding to the predictions shown in (a).

SRS, for $n = 1/3$ at room temperature. The flow stress shifts upward with increasing strain owing to strain hardening, as expected. The SRS is between 10^{-10} and $10^{-5}\,\mathrm{s}^{-1}$, m is almost zero, being dominated by aging of the mobile dislocations with a negligible forest contribution. For strain rates $>10^{-5}\,\mathrm{s}^{-1}$, the forest aging becomes more important and, at the higher strain rates, the domain of nSRS widens with increasing strain because of the increase in forest strengthening and its aging.

Temperature is an important factor in dynamic strain aging, with an influence opposite to that of the applied strain rate. The temperature influences the flow stress and its rate dependence (e.g. Eq. (18)), the solute diffusion rate (Eq. (12)), the saturation binding energy $\Delta E_\infty^{\mathrm{core}}$ (Eqs. (11), (14), (15)), the ratio $\Delta\tau_{\mathrm{m}\infty}/\tau_o$, and other secondary parameters such as the elastic modulus. The equations describing the evolution of densities of mobile and forest dislocations

may contain some temperature-dependent terms (e.g. the term representing the annihilation of mobile dislocations by cross-slip and recovery of the forest density) [7], which are incorporated in the current model by the simple variation of the parameter $\rho_{\mathrm{f}}^{\mathrm{sat}}(T)$ with temperature (Eq. (16)). With all of these factors, the predicted flow stress vs. temperature for Al–4.5%Mg alloys is shown in Fig. 4a at various levels of plastic strain (2%, 5% and 10%) and a strain rate of $10^{-3}\,\mathrm{s}^{-1}$. Also shown in Fig. 4a are the experimental data reported by Picu al. [33] for Al–Mg alloy AA5182-O. The error bars accompanying the data points at intermediate temperatures are due to the appearance of serrations in the experimental stress–strain curves. The model predicts the observed temperature dependence in generally good agreement with the experiments, exhibiting a near-linear decrease in the low-temperature regime, a threshold or slight increase in flow stress at intermediate temperatures that corresponds to the region of nSRS, and a return to a decreasing stress in the high temperature regime. The agreement in the low-temperature regime is not surprising,
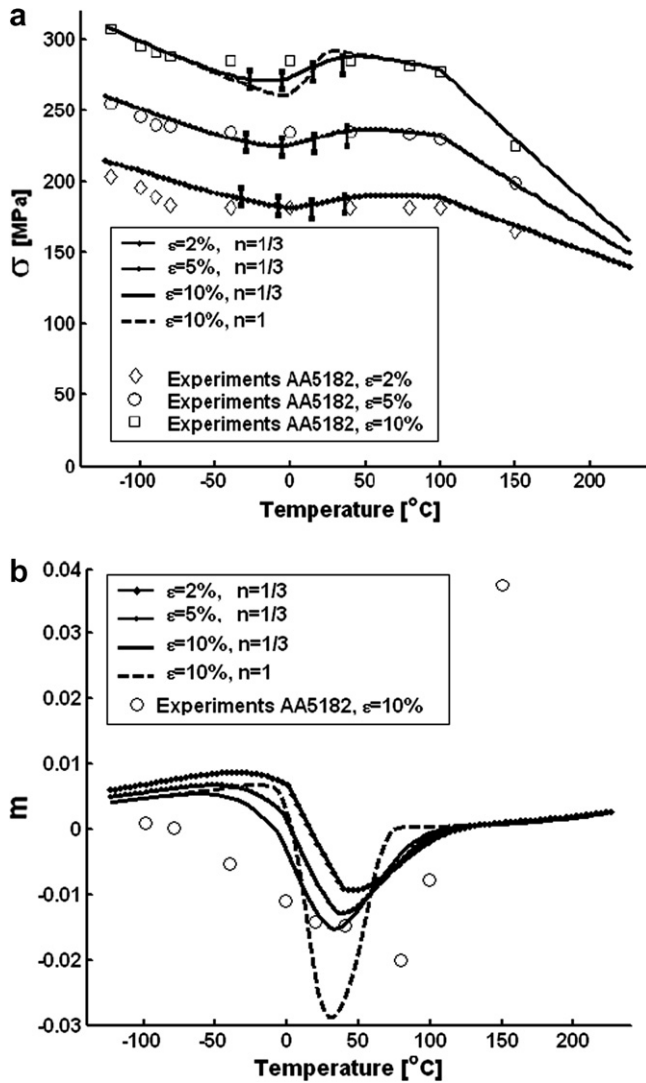
Fig. 4. (a) Tensile flow stress vs. temperature for several levels of plastic strain at $\dot{\varepsilon} = 10^{-3}$/s, as predicted (lines) and as measured (symbols) on AA5182-O [33]. (b) SRS vs. temperature for several levels of plastic strain, as predicted (lines) and as measured (symbols) on AA5182-O [33] by strain-rate jump tests via $m = \log(\tau_2/\tau_1)/\log(\dot{\varepsilon}_1/\dot{\varepsilon}_2)$ with $\dot{\varepsilon} = 10^{-3}$/s and $\dot{\varepsilon} = 10^{-3}$/s.

as one experimental stress–strain was used in this regime to obtain the forest dislocation density evolution parameters. What is noteworthy here is the prediction of the plateau/increase due to the aging mechanisms operating in the intermediate temperature range, and the general agreement with experiment. The high-temperature regime is analogous to the low strain-rate regime in Fig. 2a, and thus shows a return to decreasing flow stress with increasing temperature.

The SRS vs. temperature for AA5182-O is shown in Fig. 4b. As done experimentally, here the SRS parameter is computed using two steady-state tests at $\dot{\varepsilon}_1 = 10^{-3}$ s^{-1} and $\dot{\varepsilon}_2 = 10^{-1}$ s^{-1} as $m = \log(\tau_2/\tau_1)/\log(\dot{\varepsilon}_1/\dot{\varepsilon}_2)$. The predictions show the trends and magnitude well, but the experiments show a broader range of nSRS than predicted, with the relevant comparison being the prediction for

parameter $n = 1/3$ at 10% strain. The high SRS at the highest temperature of 150 °C is not captured well, in part owing to the high value of $\Delta\tau_{m\infty}$, but also indicating that there are other high-temperature mechanisms not represented in the model. For instance, solute drag acting on the unpinned mobile dislocations can add a positive SRS that becomes increasingly important with increasing temperature, ultimately controlling deformation at temperatures of 430–480 °C.

Fig. 5 shows the SRS vs. strain as determined using $m = \log(\tau_2/\tau_1)/\log(\dot{\varepsilon}_1/\dot{\varepsilon}_2)$ for $\dot{\varepsilon}_1 = 10^{-4}$ s^{-1} and $\dot{\varepsilon}_1 = 10^{-2}$ s^{-1}, for temperatures spanning the range from low to high. For temperatures within the DSA domain, the evolution of m with strain is not monotonic but, rather, has a minimum at a critical strain. Thus, m may have positive values at small deformations, become negative at intermediate strains, and then increase again for very large deformations. However, at a given strain, the SRS parameter decreases with temperature until a minimum value and then increases again, as also seen in Fig. 4b. Such complex behavior should present a tough test for the model. Nonetheless, the general behavior agrees with available experimental data at three temperatures [33,38], as shown in Fig. 5, with the difference at $T = 110$ °C mainly partly associated with the high value of $\Delta\tau_{m\infty}$. Similar behavior was previously captured using the forest strengthening mechanism and an additional instantaneous positive SRS contribution assumed linear in strain, with various parameters fit to experimental data [11,12]. In contrast, the results are obtained naturally from the full constitutive theory and with no fitting to the experiments aside from the estimate of $n = 1/3$.

3.2. Solute concentration dependence

Section 3.1 focused primarily on predictions as a function of the macroscopic applied variables $\dot{\varepsilon}$, ε, and T, with
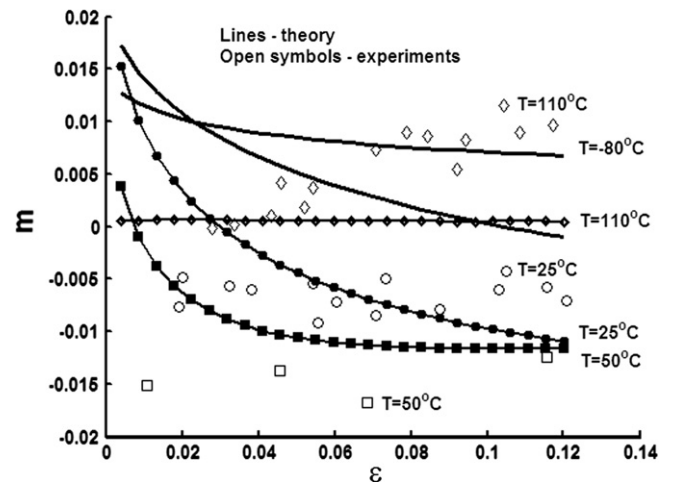

Fig. 5. SRS vs. plastic strain for various temperatures, as predicted by the model (lines) and as measured experimentally (symbols) on AA5182 [33]. Here $m = \log(\tau_2/\tau_1)/\log(\dot{\varepsilon}_1/\dot{\varepsilon}_2)$ with $\dot{\varepsilon} = 10^{-4}$/s and $\dot{\varepsilon} = 10^{-2}$/s.

some parametric variations in a few material-related parameters. This section turns to examining the dependence of DSA and nSRS on a key fundamental material parameter: the solute concentration. The solute concentration has a strong influence on a range of parameters, and thus influences the overall stress/strain/strain-rate/temperature predictions in a complex manner. The concentration scalings predicted by various components of the model are

(i) Zero temperature flow stress (Eq. (9)): $\tau_0 \propto c^{2/3}$
(ii) Zero stress energy barrier (Eq. (10)): $\Delta E_0 \propto c^{1/3}$
(iii) Saturation cross-core binding energy (Eq. (11)): $\Delta E_\infty^{core} \propto c$

The aging strengthening terms ($\Delta\tau_{m\infty}$ in Eq. (6) and δ in Eq. (7)) for both mobiles and forests are proportional to ΔE_∞^{core} and, hence, also scale linearly with concentration. A linear variation in the flow strength with concentration was experimentally observed in Al–Mg alloys [39]. Other experimental observations include an increase in the domain of Portevin–LeChatelier (PLC) instabilities with increasing solute concentration for fcc Cu–Al and Cu–Mn alloys [40–44]. Proper prediction of the concentration dependence is thus another stringent test of the model.

Fig. 6 shows the variation in the flow stress with solute concentration in binary Al–Mg, as predicted by the current model with $n = 1/3$ at $\varepsilon = 10$, $\dot{\varepsilon} = 3 \cdot 10^{-3}s^{-1}$, $T = 25\,°C$ and 150 °C. Also shown are the experimental results on Al–Mg binary alloys [35]. Theory and experiment agree well. Comparing the results at $T = 25\,°C$ and $T = 150\,°C$, the model predicts a decrease in strength that is independent of temperature, whereas the experiments suggest a greater decrease in strength at a higher concentration compared with that at a lower concentration. Recall that the only fitted data here are the stress–strain curves for pure Al at
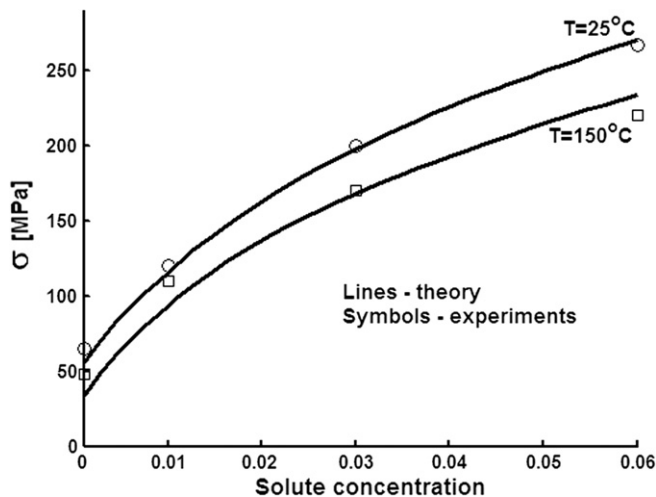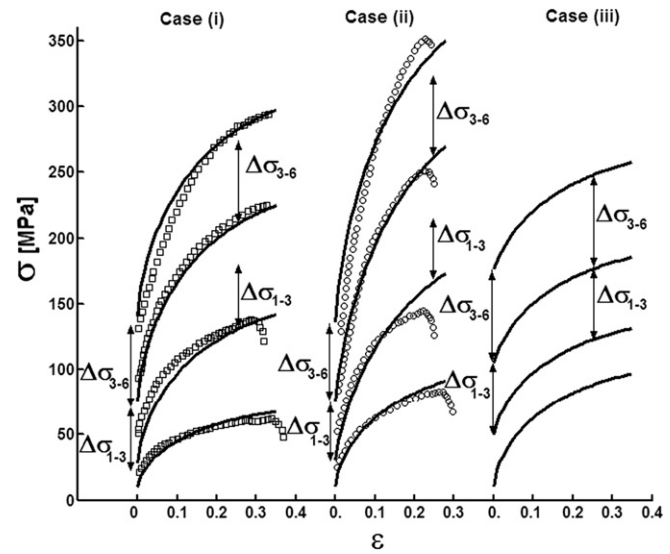

Fig. 7. Tensile stress–strain curves for pure Al and Al–Mg binary alloys with solute concentrations of $c = 1\%$, 3% and 6%, under several loading conditions: (i) $T = 150\,°C$, $\dot{\varepsilon} = 3 \cdot 10^{-3}/s$ (saturated aging); (ii) $T = 25\,°C$, $\dot{\varepsilon} = 3 \cdot 10^{-3}/s$ (within nSRS domain); (iii) $T = 25\,°C$, $\dot{\varepsilon} = 10^3/s$ (no aging). $\Delta\sigma_{1-3}$ and $\Delta\sigma_{3-6}$ are the differences in yield stress (zero plastic strain) between concentrations 1%, 3% and 3%, 6% respectively, and shown shifted out to $\varepsilon = 0.25$ to facilitate assessment of non-additivity. Cases (i) and (ii) show non-additivity of solute and forest strengthening: at any plastic strain, the difference in stresses exceeds the initial yield stress difference ($\Delta\sigma_{1-3}$ or $\Delta\sigma_{3-6}$). Case (iii) shows additivity: the difference in stresses equals the initial yield stress difference. Symbols: experiments for Al and Al–Mg binary alloys with solute concentrations of 1%, 3% and 6% solute concentration [35].

$\dot{\varepsilon} = 2.9 \cdot 10^{-3}/s$ and for the Al–3%Mg at $T = 150\,°C$ and $\dot{\varepsilon} = 2.9 \cdot 10^{-3}/s$ [35], all of which are shown in Fig. 7 along with other data on binary alloys. Thus in Fig. 6, three points have been fitted: ($c = 0\%$, $T = 25\,°C$), ($c = 0\%$, 150 °C) and ($c = 3\%$, $T = 150\,°C$). The predicted concentration follows a phenomenological power law behavior of the form $\tau = \tau(c = 0) + ac^\beta$ with exponent $\beta \sim 0.5$, i.e. a near-square-root dependence. The observation of an apparent power-law exponent thus does not provide direct insight into the mechanisms controlling rate-dependent deformation, but rather reflects a complex competition among mechanisms, none of which scales with $c^{0.5}$.

3.3. Non-additivity of strengthening mechanisms

One of the perplexing issues in deformation of fcc metals is the apparent non-additivity of solute and forest strengthening in some alloy systems. Additivity is probed by changing the solute concentration and is "expected", because the concentration is thought to change only the solute strengthening and not the work hardening. If additivity holds, stress–strain curves for different solute concentrations are related by a strain-independent vertical shift associated with the change in solute strengthening τ_0. Kocks [13] noted that non-additivity is observed in materials that also show dynamic strain aging effects (Al–Mg [45], Cu–Al [42] or Ni–Mo [46]), but at strain rates that are outside the

Fig. 6. Tensile flow stress at $\varepsilon = 10\%$ vs. Mg solute concentration, for binary Al–Mg alloys at $\dot{\varepsilon} = 3 \cdot 10^{-3}/s$, $T = 25\,°C$, 150 °C. Open symbols: as measured [35]. Lines: as predicted, with $n = 1/3$ and $\lambda = 1.87$.

range of serrated flow and nSRS. Kocks thus discounted mechanisms associated with aging. Non-additivity has been represented by various approximate forms combining solute and forest strengthening, but with limited physical underpinning.

The current model predicts non-additivity of the strengthening owing to the aging phenomena in the high-temperature and low-strain-rate regimes outside the nSRS region, as well as within the nSRS regime. The model further predicts additivity at low temperatures or high strain rates, i.e. the regimes where aging phenomena do not play a role. The origin of the non-additivity is in the strengthening of the forest mechanism due to solute diffusion, as manifested in the contribution $\bar{\tau}_f(\varepsilon)\delta(c,T)$ in Eq. (7) that depends on the temperature and solute concentration. Specifically, in the high-temperature or low-strain-rate regime, the flow stress is given by

$$\tau \cong \tau_0(c) + \bar{\tau}_f(\varepsilon)[1 + \delta(c,T)] + \Delta\tau_{m\infty}(c,T)$$
$$- \tau_0(c)\left(\frac{kT}{\Delta E_0(c)}\log\left(\frac{v_0\Omega}{\dot{\varepsilon}}\right)\right)^{1/\alpha} \quad (27)$$

where the additional forest/solute-aging interaction $\bar{\tau}_f(\varepsilon)\delta(c,T)$ adds onto the otherwise additive (rate-dependent) contributions from solutes and forests.

Proceeding quantitatively, Fig. 7 shows stress–strain curves for binary Al–Mg for three cases: (i) $\dot{\varepsilon} = 3 \cdot 10^{-3}$/s, $T = 150\,°C$, which is outside the nSRS domain but is influenced by aging due to the high temperature; (ii) $\dot{\varepsilon} = 3 \cdot 10^{-3}$/s, $T = 25\,°C$, which is inside the nSRS regime; and (iii) $\dot{\varepsilon} = 10^4$/s, $T = 25\,°C$, which is outside the nSRS and has no aging effects due to the high strain rate. Predictions are made at three solute concentrations, and cases (i) and (ii) are compared with data by Ayres [35] (no data exist for case (iii)). The predictions and experiments for pure Al are also shown for completeness. For case (iii), the stress–strain curves for different solutes are related by a vertical shift associated with the increase in solute strengthening obtained at the onset of plastic deformation, i.e. additivity holds. For case (i), the stress–strain curve for the higher concentrations shows stresses that exceed those predicted by solute strengthening alone, an effect corresponding to the strengthening of the forest mechanism by the solute diffusion. The behavior in case (i) is exactly the non-additivity observed outside the nSRS range, as pointed out by Kocks [13]. Moreover, the experimental data agree well with the model predictions, although perhaps showing a stronger degree of non-additivity. Case (ii) shows that the non-additivity exists also within the nSRS domain but, because the aging process is not saturated, the additional strength is lower than in case (i); case (ii) also differs from case (i) owing to the temperature difference. Experimental results again show excellent agreement. The present model thus explains, with no special additional mechanisms, the existence of non-additivity of strengths occurring in alloys exhibiting dynamic strain aging phenomena. Considering the results differently, the agreement with experiment is
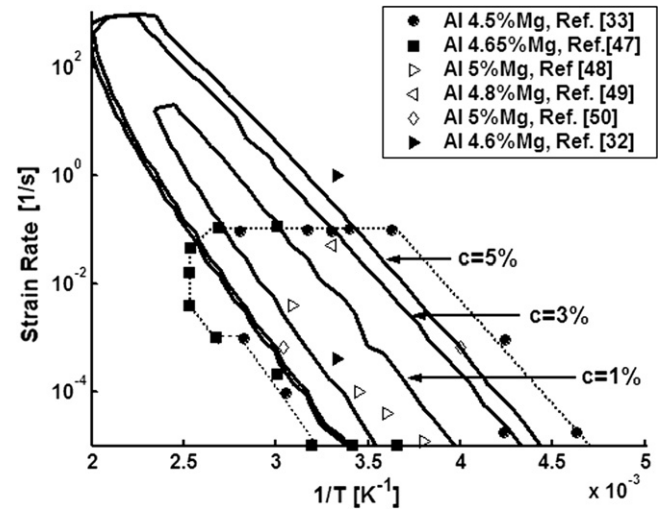

Fig. 8. Domain of nSRS in the plane of strain rate $\dot{\varepsilon}$ vs. inverse temperature $1/T$, as predicted for various solute concentrations (continuous lines) and as measured for alloys with ~5% Mg (bounded by dotted lines) for Al–Mg alloy. Model predictions use $n = 1/3$ and parameters for AA5182. The two data points of Benallal et al. [32] are also shown for completeness, but are not consistent with any other data, and suggest a domain shifted up in rate by a factor of ~10; the predictions for the Benallal et al. material and conditions were previously shown in Fig. 2 and reasonably capture the upper and lower domain boundaries at the temperature studied.

evidence that the mechanism of forest aging exists and operates in a manner consistent with the model.

3.4. Temperature/strain-rate domain of nSRS

It is common to develop temperature/strain-rate maps delineating the domain within which negative strain-rate-sensitivity occurs. As the model predicts the SRS as a function of any combination of loading parameters, it can predict this domain. Fig. 8 thus shows the domain of nSRS (actually $m \leqslant -0.001$) within the space of $\dot{\varepsilon}$ and inverse temperature $1/T$, as predicted by the model at a plastic strain of 10%, using $n = 1/3$ and for several solute concentrations. Also shown in Fig. 8 are the domain boundaries found experimentally in different studies for alloys with 4–5% Mg, but the "domain boundary" along $\dot{\varepsilon} = 10^{-5}\,s^{-1}$ is not really a limiting boundary for nSRS but, rather, the limit of available experiments. Fig. 8 also shows various experimental points lying within the nSRS domain [32,33,47–50]. The predicted and measured domains are inclined, as expected for a thermally activated process, where an increase in temperature is equivalent to a decrease in strain rate. The lateral boundaries of the nSRS domain are relatively close to, although slightly narrower than, the experimental domain. The slopes of the lateral domain boundaries agree relatively well with experiments, indicating that the model contains the correct apparent activation energies for the process. Fitting the predictions for the lateral boundaries in Fig. 8 to an Arrhenius law $\dot{\varepsilon} \sim e^{-\Delta H/kT}$ reveals apparent activation enthalpies ΔH of 0.80 eV for the lower temperature boundary and 0.98 eV

for the higher temperature boundary. These values are close to the experimental values of 0.86 and 1.09, respectively, obtained by Picu et al. [33], and are determined mainly by the enthalpy for cross-core diffusion of $\Delta H_c - \overline{\Delta W}/2 \cong 0.90$ eV. The difference in activation enthalpy between the high and low temperature boundaries arises in the model from the competition between cross-core diffusion, the rate of forest production, the underlying rate dependence of the solute strengthening, and other temperature-dependent factors in the model. Agreement along the upper boundary of the domain is poor, however, with the experiments showing a temperature-independent boundary at a strain rate of $\approx 10^{-1} – 10^0$ s^{-1}, while the theory predicts domain closure at a much higher strain rate and higher temperature. The difference in the upper limit of strain rate occurring at high temperatures $T \geqslant 100$ °C is again due, in part, to the absence of effects such as recovery, solute drag, etc., as discussed earlier and deserving of further attention. Lastly, the predicted domains for lower solute concentrations do not shrink substantially upon reduction of the concentration from 5% to 3%, but then collapses quickly upon reduction of the concentration to 1%, decreasing primarily on the low temperature side. Fig. 8 also shows the boundary obtained by Benallal et al. [32] see Fig. 2 on AA5083 at one temperature, which differs from all experimental observations. Possible reasons for the difference may be (i) that the data for AA5083 are reported at a strain of 5% or (ii) significant differences in samples preparation, which are manifest by the much higher estimated value of ρ_f^{sat}.

3.5. Transient response in strain-rate jump tests

So far, the model has been applied to predict steady-state strain-rate behavior. In actual applications, materials are subjected to non-constant loading, either intentionally or, when the nominal loading is in the nSRS range, owing to PLC-type instabilities. A full rate theory must thus also be capable of predicting the non-steady-state response of the material, including strain-rate jumps and rapid stress changes, to enable accurate and convergent simulations of material forming and loading processes. Furthermore, for many practical reasons (to avoid issues connected to the load history, to obtain extensive data from a test single specimen, etc.), the SRS parameter is often determined experimentally from strain-rate jump experiments. In these tests, a base strain rate is applied for some period of time, followed by an instantaneous jump to a second value, which is then maintained for another period of time. A sequence of jumps in strain rate, either up or down, provides valuable data on the instantaneous, transient and steady-state stress responses of the system at various strain rates and strain levels. When the strain rate is changed instantly to a new value from a prior near-steady-state condition, the magnitude of the stress change is captured by the "instantaneous" SRS m_i, which takes the value

$$m_i = \tau_0 (kT/\Delta E_0)^{1/\alpha} [(\log(v_0 \Omega / \dot{\varepsilon}_2))^{1/\alpha}$$
$$- (\log(v_0 \Omega / \dot{\varepsilon}_1))^{1/\alpha}] \qquad (28)$$

With time, the stress then relaxes to the steady-state value corresponding to the post-jump strain rate. The convergence is always "from above", i.e. the instantaneous stress is higher than the steady-state stress for an increase in the strain rate, and "from below", i.e. instantaneous stress is lower than the steady-state stress for a decrease in the strain rate. This general behavior was examined in the companion paper considering mobile dislocation aging only, and is contained in the current model as shown below.

So far in this paper, the main phenomenon of nSRS has been controlled by the forest aging mechanism. However, mobile aging mechanism is of paramount importance in the transient behavior. Specifically, the mobile aging mechanism controls the instantaneous SRS and the initial transient stress relaxation. Thus, while steady-state nSRS can be obtained without mobile aging, mobile aging must exist to obtain the correct transient behavior. The inability of forest aging to give the observed behavior can be understood conceptually as follows. As the forest mechanism depends on the forest density, which in turn depends only on the plastic strain evolution, a jump in strain rate does not change the plastic strain or the forest density or the forest strengthening. Only as the material continues to accumulate strain at the post-jump strain rate can the forest mechanism change the flow stress. To reach steady-state at the post-jump strain rate requires that the forest aging evolve to the appropriate value. For a jump down in strain rate, the rate of production of new forest dislocations is slowed, and the average forest aging time increases. For a jump up in strain rate, the production of new forest dislocations is accelerated, and so the average forest is younger and less-aged. To reach steady-state requires waiting long times, and thus large strains, for the forests to age. The transient time or strain to achieve steady state is thus very long, and the transient strain needed can exceed the ductility of the specimen, i.e. steady-state is not achieved. This situation is not reported experimentally, and an instantaneous positive SRS $m_i > 0$ is the norm. Thus, mobile aging is essential to a proper understanding of the entire scope of aging phenomena. The paper now turns to some specific results demonstrating this qualitative discussion.

The sequence of jump tests reported by Picu and collaborators [51], from whom the full data set was obtained, is simulated exactly. The test corresponds to multiple jumps in strain rate back and forth between the values of 10^{-3} s^{-1} and 10^{-4} s^{-1} at room temperature in Al–Mg 5182. At both strain rates, the material is in the nSRS range, such that the steady-state stress–strain curve for $\dot{\varepsilon}_2 = 10^{-3}$ s^{-1} lies below the steady-state curve for $\dot{\varepsilon}_1 = 10^{-4}$ s^{-1}. The material also exhibits serrated flow, which will not appear in the prediction because the model is for material elements undergoing imposed spatially
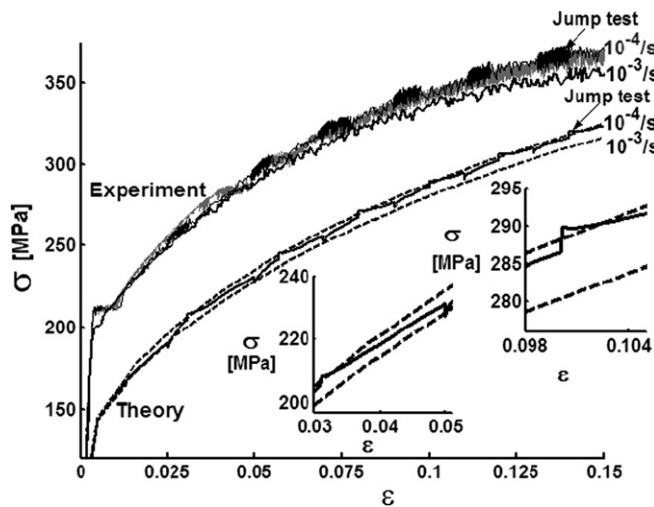
Fig. 9. Tensile stress–strain curves for steady-state strain rates $10^{-4}\,\text{s}^{-1}$ and $10^{-3}\,\text{s}^{-1}$ and for a strain-rate-jump test corresponding to multiple instantaneous jumps from $10^{-4}\,\text{s}^{-1}$ to $10^{-3}\,\text{s}^{-1}$ and the reverse, as measured on AA5182 [51] (shifted up by 50 MPa for clarity) and as predicted by the present model. Insets: detail around strain-rate jumps at 3–5% strain and 10% strain. For both experiment and model, the transient for a jump down from $10^{-3}\,\text{s}^{-1}$ to $10^{-4}\,\text{s}^{-1}$ is rapid, while the transient for a jump up from $10^{-4}\,\text{s}^{-1}$ to $10^{-3}\,\text{s}^{-1}$ is significantly slower and convergence to the steady state at $10^{-3}\,\text{s}^{-1}$ is not attained prior to the imposition of the subsequent jump down to $10^{-4}\,\text{s}^{-1}$. The stress–strain curve for the jump tests thus stays close to the steady-state curve at rate $10^{-4}\,\text{s}^{-1}$.

homogeneous deformation. Fig. 9 shows the steady-state stress–strain curves for the two constant-rate tests and the stress–strain curve obtained for the sequence of jumps in the strain rate consisting of a jump from $10^{-3}\,\text{s}^{-1}$ to $10^{-4}\,\text{s}^{-1}$ at 2.5% strain, from $10^{-4}\,\text{s}^{-1}$ back to $10^{-3}\,\text{s}^{-1}$ at 3.1%, and then alternating jumps at 5, 5.7, 7, 8, 9, 10, 11, 12, 13 and 14% deformation. Surprisingly, the experiments show that, on average, the stress–strain curve in the jump test experiment nearly overlaps that for the steady-state behavior for the lower rate of $\dot{\varepsilon}_1 = 10^{-4}\,\text{s}^{-1}$. Jumps up to $\dot{\varepsilon}_2 = 10^{-3}\,\text{s}^{-1}$ are accompanied by an instantaneous jump above the steady-state stress for $\dot{\varepsilon}_1 = 10^{-4}\,\text{s}^{-1}$ followed by larger serrations and a relaxation of the stress, but the stress level does not approach anywhere near the steady-state level for rate $\dot{\varepsilon}_2 = 10^{-3}\,\text{s}^{-1}$. Although not at all the "expected" behavior according to traditional models, the model explains this behavior, as follows.

Fig. 9 shows the stress–strain curves predicted by the model for the two steady-state rates $\dot{\varepsilon}_1 = 10^{-4}\,\text{s}^{-1}$ and $\dot{\varepsilon}_2 = 10^{-3}\,\text{s}^{-1}$, and for the strain-rate jump test. The model uses the full time-dependent rate theory in Eqs. (1b) and (1c) with the other constitutive behavior described earlier; there are no additions or changes to any material parameters. The model predicts that, for the jumps from $10^{-4}\,\text{s}^{-1}$ to $10^{-3}\,\text{s}^{-1}$, there is a small instantaneous stress jump up followed by a short transient and then a subsequent longer transient. During the period between 3.1% and 5%, the model predicts that the stress can relax nearly to the steady-state stress for $10^{-3}\,\text{s}^{-1}$ at 5% strain. For the subsequent jump down in strain rate from $10^{-3}\,\text{s}^{-1}$ to $10^{-4}\,\text{s}^{-1}$ at

5% strain, there is a small instantaneous stress decrease followed by a short transient and then a longer transient, but this longer transient is much faster than that for the jump up in strain rate at 3.1%. Thus, the stress nearly recovers to the steady-state $10^{-4}\,\text{s}^{-1}$ value by the time a jump up in strain rate is imposed at 5.7% strain. Subsequent jumps at $\sim$1% strain increments show that, for jumps down in strain rate, the material is unable to reach the steady-state $10^{-3}\,\text{s}^{-1}$ stress level prior to the imposition of the subsequent jump back down to $10^{-4}\,\text{s}^{-1}$. The overall stress level thus remains very close to the stress corresponding to steady state at $10^{-4}\,\text{s}^{-1}$. The jumps down in rate occur at stresses already close to the steady state rate at $10^{-4}\,\text{s}^{-1}$ and thus show much shorter transients. This behavior, which was computed prior to the availability of the detailed experimental results, is in remarkable quantitative agreement with the experiments. The agreement between the experiment and model for the jump test arises precisely because there is an instantaneous jump and short transient owing to the solute aging, and high asymmetry in the longer transient response of the forest dislocation aging. Jumps down in rate relax comparatively quickly, while jumps up in rate relax comparatively slowly. This is yet another strong confirmation that the mechanisms contained in the model are physically correct and essential to the dynamic strain aging phenomenon.

4. Discussion and summary

This section briefly discusses aspects of the model with respect to previous models, other potential models and experiments, and then summarizes the work.

The collection of equations constituting the present theory appears similar to sets of equations proposed in the recent literature, e.g. Ref. [28]. Those models include some type of underlying rate-dependent phenomena, presumably solute strengthening, but not explicitly stated, a backstress due to forest dislocation strengthening that evolves with dislocation density but does not contain aging, and a solute-related aging stress that is of the form of Eq. (6). However, these models remain phenomenological in that: (i) the solute-related aging stress is introduced "by hand" to ensure nSRS; (ii) the rate theory is an approximate, steady-state-type model that is augmented by an ad hoc evolution of an aging time parameter, as proposed by McCormick, and does not recognize the key fact brought forth in the companion paper showing that nSRS cannot arise from considering solute effects on the mobile dislocations alone; (iii) the models do not identify any specific aging mechanism(s); (iv) there is no fundamental basis for the values of the many phenomenological parameters employed in the theory; and hence (v) quantitative success relies on fitting of a number of key parameters, such as the rate-dependence of the aging and the saturation magnitude of the aging strength, to experiments. These theories and others [3,4,52] can show many of the complex dynamic phenomena associated with DSA and nSRS, but such

complex dynamics may emerge simply from the fact that the equations are fundamentally unstable over a range of strain rates, owing to the introduction of nSRS by construction in the governing equations. In contrast, the present theory is mechanistically based, uses microscopically derived material parameters, and has been shown to be quantitatively predictive.

One could question the choice of the solute strengthening process as the underlying rate-controlling process, and whether the theory would be modified under other circumstances. The solute strengthening process was chosen for three reasons. First, the simple 1D model of two competing rate processes shows that the small-scale process controls the rate dependence. Second, the solute strengthening operates at all plastic strain levels, in contrast to the forest strengthening mechanism, which is small at small plastic strains. If the forest mechanism were chosen to be the controlling rate phenomenon, the theory would most likely require that both rate mechanisms be considered simultaneously with some transition in dominance occurring with increasing plastic strain. Third, the rate sensitivity of forest hardening is generally known to be extremely small, owing to the large energies associated with junction formation. In the calculations of Picu, the energy barriers relevant for the forest strengthening were also found to be large such that resolved stresses very close to the zero-temperature strength are required to reduce the energy barriers to levels low enough for thermal activation at experimental rates [51]. Nonetheless, a theory with structure very similar to the present theory can be formulated by considering the forest mechanism to be the rate-controlling mechanism, with solute strengthening acting as the back stress. In such a case, the energy barrier would still take a form analogous to Eqs. (3) and (4), i.e.

$$\Delta E(\tau, t) = \frac{\Delta E_{0f}}{kT} \left(1 - \frac{\tau_{eff}(t)}{\bar{\tau}_f(\varepsilon)} \right)^{\alpha} \qquad (29)$$

$$\tau_{eff}(t) = \tau_{app}(t) - \Delta\tau_{am}(t - t_p) - \Delta\tau_f(t, \varepsilon) \qquad (30)$$

where the energy ΔE_{0f} is the barrier for the junction-breaking process, and $\bar{\tau}_f(\varepsilon)$ is the zero-temperature junction strength as before. The mobile solute aging strength and forest aging strength again enter as backstresses, even though the mechanisms have switched roles. As the only quantity that depends on the pinning time is still the mobile solute aging term, the resulting theory is nearly identical in structure to the one proposed here. The difference is that the parameters ΔE_{0f} and $\bar{\tau}_f(\varepsilon)$ for forest strengthening replace the analogous quantities ΔE_0 and τ_0 relevant for solute strengthening. Eqs. (29) and (30) without $\Delta\tau_{am}(t - t_p)$ would essentially be a rate form of the Picu et al. model in which forest strengthening and aging are the only mechanisms.

Regarding strain-rate jump experiments, such tests have been performed and carefully analyzed by Schwink et al. in different alloys [42,43,53,54]. These tests were performed outside the domain of nSRS, at very low strain rates, so that stable deformation is obtained at all strain rates used. They observe the classic instantaneous stress jump followed by a transient relaxation to the steady-state stress prevailing at the post-jump rate. Such behavior may arise because the experiments are outside the regime of nSRS, where the magnitude of the aging effects may be very small, and the forest aging may be near saturation at all times. Thus, these experiments may be dominated by the mobile solute aging mechanism, which exhibits all the classic behaviors as shown in the companion paper, rather than by the behavior predicted here and observed in the experiments [33] in the nSRS domain.

The present model also qualitatively rationalizes the absence of nSRS effects in precipitate-strengthened alloys, such as Al–6XXX, Al–Cu, and Al–Li. In such alloys in the aged condition, there is often a solute strengthening contribution in addition to the precipitate-strengthening. If solute strengthening alone were able to generate nSRS, such behavior would then be anticipated in these alloys. However, it was shown in the companion paper that nSRS cannot occur for solute strengthening alone, and here the nSRS is attributed to aging of the forests and its consequences on junction strength. As forest strengthening is less important, and perhaps negligible, in precipitate-strengthened alloys, the present theory suggests that nSRS should not occur in such systems. This qualitative conclusion is consistent with the experimental literature but is certainly not definitive. Furthermore, nSRS could be observed in such systems if there was a solute-aging effect on the precipitate strengthening mechanism, e.g. diffusion of solutes to the precipitate interface, modifying the strengthening by changing the antiphase boundary energy or some feature of Orowan looping, but such mechanisms have not been considered or explored. This is an area for future work.

In summary, a full rate-dependent constitutive theory for dynamic strain aging was developed, based on the idea that a single physical aging mechanism, cross-core diffusion within a dislocation core, influences both solute strengthening and forest strengthening mechanisms. It was shown that all the key parameters in the model, apart from forest dislocation evolution parameters, are derivable from atomistic-scale material parameters, so that the theory contains essentially no adjustable parameters. It was then shown that, in application to a variety of Al–Mg alloys, the model predicts the steady-state stress/strain/strain-rate/temperature/concentration dependent material response, in qualitative and quantitative agreement with available experiments. The model also reveals the origin of non-additivity of solute and forest strengthening and explains the transient behavior observed in strain-rate jump tests. The theory thus provides a complete, mechanistically based, predictive model for dynamic strain aging, which constitutes a major advance in the understanding of solute-strengthened metal alloy systems.

Acknowledgments

Appendix A

Following a procedure similar to the method described in Appendix 1 of the companion paper, one can obtain an analytic model for the constitutive behavior in steady state. The computed quantity is the average waiting time $\bar{t}_w$, which is then related to the strain rate via $\bar{t}_w = \Omega(\varepsilon)/\dot{\varepsilon}$. $\bar{t}_w$ can be written in the following form:

$$\bar{t}_w = t_0 D_0 + t_1 D_1 + t_\infty D_\infty \tag{A1}$$

where

$$t_0 = \left(v_0 \exp\left(-\frac{\Delta E_0}{kT} \left(1 - \frac{\tau - \Delta \tau_f}{\tau_0} \right)^\alpha \right) \right)^{-1}$$

$$t_1 = \left(v_0 \left(1 + \frac{n}{n+1} 0.36\alpha \left(1 - \frac{\tau - \Delta\tau_f}{\tau_0} + 0.63\frac{\Delta\tau_\infty}{\tau_0} \right)^{\alpha-1} \frac{\Delta\tau_\infty}{\tau_0} \frac{\Delta E_0}{kT} \right) \right)^{-1}$$
$$\times \exp\left(\frac{\Delta E_0}{kT} \left(1 - \frac{\tau - \Delta\tau_f}{\tau_0} + 0.63\frac{\Delta\tau_\infty}{\tau_0} \right)^\alpha \right)$$

$$t_\infty = \left(v_0 \exp\left(-\frac{\Delta E_0}{kT} \left(1 - \frac{\tau - \Delta\tau_f}{\tau_0} + \frac{\Delta\tau_\infty}{\tau_0} \right)^\alpha \right) \right)^{-1}$$
$$\tag{A2}$$

and with

$$D_0 = 1 - \exp\left(-(1-k)\frac{t_d}{t_0} \right)$$
$$D_\infty = \exp\left(-(1-k)\frac{t_d}{t_0} - 2k\frac{t_d}{t_1} \right)$$
$$D_1 = 1 - D_0 - D_\infty,$$

The parameter k can be any number between 0 and 1 but, as observed in Appendix 1 of the companion paper [1], a value of $k = 0.95$ can lower the error to <3.5%. The stress opposing the dislocation motion due to aging on the forest dislocation $\Delta\tau_f$ is given by Eq. (7).

References

[1] Soare MA, Curtin WA. Acta Mater 2008.
[2] Cottrell AH, Stokes RJ. Proc Royal Soc London. Series A, Math Phys Sci 1955;233:17.
[3] McCormick PG. Acta Metall 1972;20:351.
[4] McCormick PG. Scripta Metall 1987;12:197.
[5] Beukel A, Kocks UF. Acta Metall 1982;30:1027.
[6] Kubin LP, Estrin Y. Acta Metall Mater 1990;38(5):697.
[7] Kubin LP, Estrin Y. Phys Stat Sol(b) 1992;172:173.
[8] Ananthakrishna G. Mat Sci Eng A 2005;400–401:210.
[9] Rizzi E, Hähner P. Int J Plasticity 2004;20:121.
[10] Curtin WA, Olmsted DL, Hector LG. Nature Mater 2006;5:875.
[11] Picu RC. Acta Mater 2004;52:3447.
[12] Soare MA, Picu RC. Int J Multiscale Comp Eng 2005;3(4):415.
[13] Kocks UF. Metal Trans A 1985;16A:2109.
[14] Kocks UF, Argon AS, Ashby MF. Prog Mat Sci 1975;19:1.
[15] Hähner P. Mat Sci Eng A 1996;207:208.
[16] Hähner P. Mat Sci Eng A 1996;207:216.
[17] Olmsted DL, Hector LG, Curtin WA. J Mech Phys Sol 2006;54:1763.
[18] Van den Beukel A. Phys Stat Sol A 1975;30:197.
[19] Balík J, Lukáč P. Acta Metall Mater 1993;41:1447.
[20] Fujikawa SI, Takada Y. Defect Diff Forum 1997;143–147:409.
[21] Picu RC, Zhang D. Acta Mater 2004;52:161.
[22] Ananthakrishna G, Valsakumar MC. Phys Lett 1983;95A:69.
[23] Amodeo RJ, Ghoniem NM. Phys Rev B 1990;41:6958.
[24] Fivel MC, Gosling TJ, Canova GR. Model Simul Mater Eng 1996;4: 581.
[25] Rodney D, Phillips R. Phys Rev Lett 1999;82:1704.
[26] Shenoy VB, Kukta RV, Phillips R. Phys Rev Lett 2000;84:1491.
[27] Ananthakrishna G. Physics Rep 2007;440:113.
[28] Fressengeas C, Beaudoin AJ, Lebyodkin M, Kubin LP, Estrin Y. Mat Sci Eng A 2005;400–401:226.
[29] Kocks UF. J Eng Mater Tech (Trans ASME Series H) 1976;98:76.
[30] Labusch R. Phys Stat Sol 1970;41(2):569.
[31] Zaiser M. Philos Mag A 2002;82:2869.
[32] Benallal A, Berstad T, Borvik T, Clausen AH, Hopperstad OS. Eur J Mech A/Solids 2006;25:397–424.
[33] Picu RC, Vincze G, Ozturk F, Gracio JJ, Barlat F, Maniatty AM. Mat Sci Eng A 2003;390:334.
[34] Krajewski PE. The warm ductility of commercial aluminum sheet alloys. Report to GM R&D and planning; 2005.
[35] Ayres RA. Metall Trans A 1978;10:849.
[36] Balik J. Mat Sci Eng 2001;A316:102.
[37] Hähner P, Ziegenbein A, Rizzi E, Neuhäuser H. Phys Rev B 2002:65. 134109-1-20.
[38] Van den Brink SH, Van den Beukel A, McCormick PG. Phys Stat Sol A 1975;30:469.
[39] Wycliffe P, Kocks UF, Embury JD. Scripta Metall 1980;14:1349.
[40] Nortmann A, Schwink Ch. Acta Mater 1997;45:2043.
[41] Nortmann A, Schwink Ch. Acta Mater 1997;45:2051.
[42] Schwink Ch, Nortmann A. Mat Sci Eng A 1997;234:1.
[43] Schwink Ch, Nortmann A. On the physical parameters governing the flow stress of solid solutions in a wide range of temperatures. In: Steck E, Ritter R, Peil U, Ziegenbein A, editors. Plasticity of metals, vol. 5. Weinheim: Wiley-VCH; 2001. p. 90.
[44] Kalk A, Nortmann A, Schwink Ch. Philos Mag A 1995;72:1239.
[45] Horvath G, Chinth NQ, Lendvai J. J Mater Res 2005;20:331.
[46] Bloom TA, Kocks UF, Nash P. Acta Metall 1985;33:265.
[47] Abbadi M, Hahner P, Zeghloul A. Mat Sci Eng A 2002;337:194.
[48] Pink E, Grinberg A. Acta Metall 1982;30:2153.
[49] Kral R, Lucak P. Mat Sci Eng A 1997;234:786.
[50] Kumar S. Scripta Metall Mater 1995;33:81.
[51] Picu RC. Private communications.
[52] Ling CP, McCormick PG. Acta Metall Mater 1990;38:2631.
[53] Carlone M, Saimoto S. Exp Mech 1996;36(4):360.
[54] Saimoto S, Cao S, Mishra RK. Mat Sci Forum 2005;421:475–9.